Bias dependent spin injection into graphene on YIG through bilayer hBN tunnel barriers

Leutenantsmeyer, J. C.; Liu, T.; Gurram, M.; Kaverzin, A. A.; Wees, B. J. van

Published in:
Physical Review B

DOI:
10.1103/PhysRevB.98.125422

Publication date:
2018

Bias-dependent spin injection into graphene on YIG through bilayer hBN tunnel barriers

Johannes Christian Leutenantsmeyer,* Tian Liu, Mallikarjuna Gurram, Alexey A. Kaverzin, and Bart J. van Wees
Physics of Nanodevices, Zernike Institute for Advanced Materials, University of Groningen, 9747 AG Groningen, The Netherlands

(Received 16 July 2018; revised manuscript received 5 September 2018; published 24 September 2018)

We study the spin injection efficiency into single and bilayer graphene on the ferrimagnetic insulator yttrium-iron-garnet (YIG) through an exfoliated tunnel barrier of bilayer hexagonal boron nitride (hBN). The contacts of two samples yield a resistance-area product between 5 and 30 kΩ μm^2. Depending on an applied dc bias current, the magnitude of the nonlocal spin signal can be increased or suppressed below the noise level. The differential spin injection efficiency reaches values from -60% to $+25\%$. The results are confirmed with both spin valve and spin precession measurements. The proximity induced exchange field is found in single layer graphene on YIG to be (85 ± 30) mT and in bilayer graphene on YIG close to the detection limit. Our results show that the exceptional spin injection properties of bilayer hBN tunnel barriers reported by Gurram *et al.* [Nat. Commun. **8**, 248 (2017)] are not limited to fully encapsulated graphene systems but are also valid in graphene/YIG devices. This further emphasizes the versatility of bilayer hBN as an efficient and reliable tunnel barrier for graphene spintronics.

DOI: 10.1103/PhysRevB.98.125422

I. INTRODUCTION

The combination of graphene with other two-dimensional (2D) layered materials is an elegant way to create atomically thin devices with adjustable properties [1–4]. The crystalline insulator hexagonal boron nitride is an appealing material for the field of graphene spintronics [5]. Its atomic flatness and sufficiently strong van der Waals interaction with graphene allows the fabrication of heterostructures of 2D materials with minimized contamination, implying good spin transport properties. A long spin diffusion length of 30 μm has been experimentally achieved in graphene where a bulk flake of hBN was used as a protective layer to avoid contamination during the fabrication process [6]. Therefore, the use of hBN as a pinhole-free tunnel barrier is straightforward since these fully encapsulated graphene devices suggest minimized contamination and highly efficient spin transport. Several experimental studies have investigated the spin injection through tunnel barriers of exfoliated hBN [7,8] and large scale hBN grown via chemical vapor deposition [9–12]. However, the experimentally demonstrated spin transport lengths are still far below the values suggested by the low intrinsic spin-orbit coupling of graphene [13].

Having graphene in proximity to magnetic materials is a novel approach to tune the intrinsic properties of graphene. Magnetic graphene is characterized by the induced exchange field [14–19]. First-principle calculations of idealized systems with superlattice matching predict an exchange splitting of the graphene spin states to exceed several tens of meV [20,21]. However, the experimentally demonstrated exchange fields [14,15,22] are still several orders of magnitude below, which can indicate either an imperfect [23] or a nonepitaxial interface between graphene and YIG or both.

The realization of graphene devices with a large exchange field requires the tackling of several challenges. The cleanliness of the interface between graphene and YIG is crucial to obtain a strong exchange effect as indicated by the discrepancy between experimentally achieved values and theoretical predictions. Furthermore, the interface and tunnel barrier between the graphene flake and contacts are crucial for the injection of a large spin accumulation and the observation of large spin signals. In our previous works we employed tunnel barriers of oxidized titanium or aluminum to overcome the conductivity mismatch problem [24,25]. For these types of tunnel barrier the magnitude of the spin signal is limited by pinholes and resulted in a relatively small spin signal of mostly less than 1 Ω, which often did not exceed the electrical noise of the measured signals in the sample. In addition, the contamination arising from the PMMA-based fabrication procedure affects the graphene cleanliness negatively. For this study we replace the Al_2O_3 or TiO_2 tunnel barrier with a bilayer-hBN (bl-hBN) flake, which significantly improves the sample quality and spin signal. Furthermore, we confirm the tunable spin injection reported by Gurram *et al.* [26] for the graphene/YIG system. While the origin of the dc bias dependence is still unclear, recent reports exclude local gating underneath the contact and carrier drift [27,28].

II. SAMPLE PREPARATION AND CONTACT CHARACTERIZATION

Thin hBN flakes are exfoliated from hBN crystals (HQ Graphene) onto 90 nm SiO_2 wafers. The thickness of the flakes is estimated through their optical contrast, which is calibrated by atomic force microscopy. In our microscope (Zeiss Axio Imager.A2m with an EC Epiplan-Neofluar 100x/0.9 objective) bl-hBN corresponds to 2.5% contrast in the green channel. Suitable bl-hBN flakes are picked up by using a dry polycarbonate based transfer method [29] and combined with

*j.c.leutenantsmeyer@rug.nl

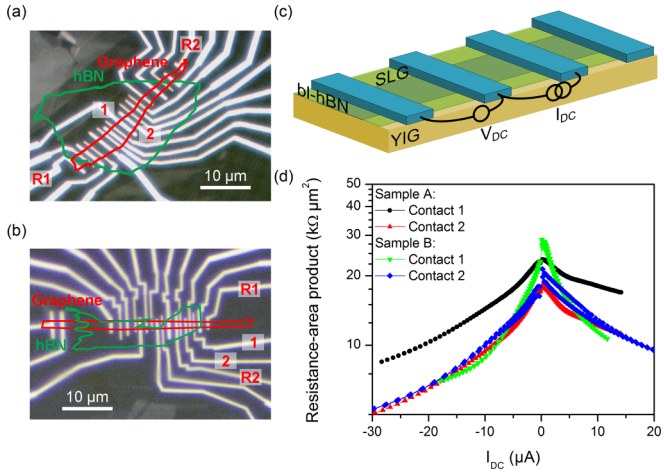

FIG. 1. (a) Optical micrograph of sample A. The outer electrodes (R) are not covered by bl-hBN and used as reference electrodes in both local and nonlocal measurements. (b) Optical micrograph of sample B. (c) Schematic measurement of the three-terminal contact resistance. (d) All working contacts have a calculated resistance-area product between 5 and 30 kΩ μm^2. The full set of IV characteristics is shown in the Supplemental Material [30].

single (sample A) or bilayer graphene (sample B) exfoliated from HOPG crystals (ZYB grade, HQ Graphene). The stack is placed on a cleaned 12 μm YIG grown by liquid phase epitaxy (LPE) on a 600 μm gadolinium-gallium-garnet substrate (Matesy GmbH). Before the transfer, the YIG substrate for sample A is treated with oxygen plasma to remove organic contaminants and annealed in a 500 °C furnace in an oxygen atmosphere prior to the transfer of the graphene/bl-hBN stack. The substrate of sample B underwent an additional argon plasma treatment before the annealing step [23].

The polycarbonate is dissolved in chloroform and the bl-hBN/graphene/YIG stack is cleaned in acetone, isopropanol, and sequent annealing for 1 h at 350 °C in an argon-hydrogen atmosphere. Contacts are defined using a standard PMMA-based electron beam lithography process. To obtain different coercive fields and switch the electrodes independently, the width of the contacts ranges between 250 and 500 nm. 45 nm cobalt and a 5 nm aluminum capping layer are evaporated at pressures below 10^{-7} mbar. After the liftoff in warm acetone, the sample [Figs. 1(a) and 1(b)] is loaded into a cryostat and kept in vacuum during the characterization. All measurements are carried out at 75 K.

After loading into the cryostat of the measurement setup, the samples are cooled down to liquid nitrogen temperature and the contacts are characterized in a three-terminal geometry [Fig. 1(c)] using the outermost contacts as reference electrodes. The resistance-area product is calculated from the current-voltage characteristics and shown for sample A in Fig. 1(d). The contacts on samples A and B which employ a bl-hBN tunnel barrier yield a typical resistance-area product between 5 and 30 kΩ μm^2, a range comparable to the one reported in Ref. [26]. An hBN covered graphene Hall bar sample fabricated in parallel with sample B for comparison yields a carrier density of $n = 5 \times 10^{12}$ cm^{-2} and a mobility of $\mu = 5400$ cm^2/V s. We found $\mu = 720$ cm^2/V s (estimated via the Shubnikov–de Haas oscillations) in our previous work [14] and conclude that the protective hBN layer significantly improves the graphene charge transport properties on YIG.

III. BIAS-DEPENDENT SPIN INJECTION THROUGH BILAYER HBN TUNNEL BARRIERS INTO SINGLE AND BILAYER GRAPHENE ON YIG

We now discuss the spin transport in graphene on YIG with a bl-hBN tunnel barrier in a nonlocal geometry [Fig. 2(a)]. A current of $I_{ac} = 1$ μA is sourced and modulated with 3.7 Hz between contacts 2 and R2. The ferromagnetic electrode injects a spin current into the graphene underneath contact 2. These spins are diffusing along the graphene channel and are probed by a lock-in as a voltage difference V_{NL} between the detector contact 1 and the reference electrode R1. Using this technique, we can decouple charge and spin transport. The signal can be defined as nonlocal resistance and calculated via $R_{NL} = V_{NL}/I_{ac}$. To characterize the basic spin transport properties of the samples an in-plane magnetic field parallel to the electrodes (B) is applied to switch the magnetization of the injector and detector [Fig. 2(a)]. Depending on the relative magnetization alignment of the injector and detector electrodes, the nonlocal resistance changes between the parallel and the antiparallel resistance states when the contact magnetization switches. This measurement represents a characteristic spin valve behavior [Figs. 2(b) and 2(c)] and gives an estimation of the spin relaxation length in the graphene flake [Fig. 2(d)].

To study the effect of the bias on the spin injection, we apply a dc current additionally to the ac current sourced between the injector and reference electrode [Fig. 2(a)]. The dielectric

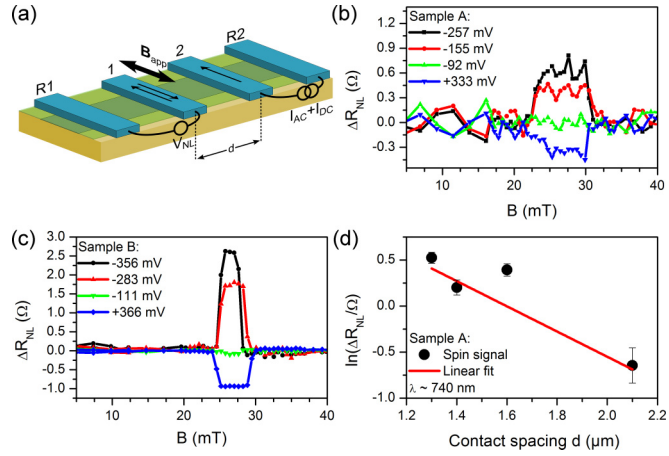

FIG. 2. (a) Schematic setup for a nonlocal spin valve measurement. (b) nonlocal spin valve measurements of sample A (bl-hBN/graphene, $\lambda \sim 740$ nm). The size of the switch between parallel and antiparallel states of contacts 1 and 2 can be tuned with the applied dc bias and is shown for four different values. (c) Sample B (bl-hBN/bl-graphene, $\lambda \sim 2.3$ μm) shows a comparable dependence on the applied dc bias. Note that the spin signal changes the sign around −92 mV. (d) The distance-dependent spin valve measurements of sample A allow the estimation of the spin relaxation length from the slope of the linear fit. The same analysis for sample B is discussed in the Supplemental Material [30].

strength of hBN is approximately 1.2 V/nm [31]. Therefore, we limit the dc bias current for sample A to 20 μA, which corresponds to 0.4–0.6 V, depending on the IV characteristics of the injector contact. To compare different contacts, we calculate the equivalent voltage V_{hBN} across the hBN tunnel barrier from the applied dc bias current and discuss all results plotted as function of V_{hBN}.

Figure 2(b) contains the spin valve measurements of sample A for four different dc bias currents over distance $d = 1.6$ μm. While no spin signal above noise level is visible at -92 mV, a dc bias current of $+333$ mV results in a clear switching between parallel and antiparallel states with a spin signal of approximately 0.4 Ω. Beyond -92 mV, we find an inverted sign of the nonlocal resistance switching and a spin signal of -0.4 Ω at -155 mV and -0.7 Ω at -257 mV.

Four spin valve measurements of sample B are shown in Fig. 2(c), where we find compared to sample A a larger spin signal of up to -2.5 Ω at -356 mV dc bias. The change of the sign of the spin signal occurs in sample B also between -100 and 0 mV, a similar range as in the measurements on sample A.

The distance dependence of the spin signal is shown for sample A in Fig. 2(d), from which we extract the spin relaxation length $\lambda \sim (740 \pm 570)$ nm. In our previous work we found a comparable value of $\lambda = (490 \pm 40)$ nm for a not hBN protected sample. We conclude that even though the charge transport properties have improved significantly, the spin transport parameters remain similar. The same analysis was applied to sample B, where we found $\lambda \sim (2.3 \pm 1)$ μm [30].

The bl-hBN tunnel barriers in Fig. 2(d) show a less clear trend in the distance dependence, resulting in a larger error in λ. We can attribute this to two origins: an inhomogeneity of the bl-hBN tunnel barriers and an inhomogeneity in the graphene flake. Microscopic cracks in the hBN tunnel barrier could arise during the fabrication and could lead to a different spin polarization of each contact. This interpretation is also supported by the considerable spread of the resistance-area product of between 5 and 30 kΩ μm^2. As a consequence, the values for the spin relaxation length extracted from the distance-dependent measurements can only be seen as an approximation. However, the consistency with the spin precession measurements as discussed in the following sections confirms the validity of the estimation.

To extract the dc bias dependence of the spin injection polarization in the cobalt/bl-hBN/graphene/YIG system, we align the magnetization of injector and detector parallel or antiparallel and sweep the dc bias current. $\Delta R_{\mathrm{NL}} = R_{\mathrm{NL}}(\mathrm{P}) - R_{\mathrm{NL}}(\mathrm{AP})$ is calculated and yields the pure spin signal of samples A and B shown in Figs. 3(a) and 3(b). For comparison, both curves are plotted as a function of V_{hBN}. While both positive and negative dc biases lead to an enhanced spin injection, a sign change at approximately -80 mV is observed. To extract the bias dependence of the spin injection polarization, we use the unbiased nonlocal spin signals to calculate the average spin polarization ($\sqrt{P_{\mathrm{I}} P_{\mathrm{D}}}$) of injector P_{I} and detector P_{D}. This assumption is justified by the similar shape of the nonlocal resistances in Figs. 3(a) and 3(b), when injector and detector contacts are swapped. This suggests a similar behavior of both contacts. We can extract a spin

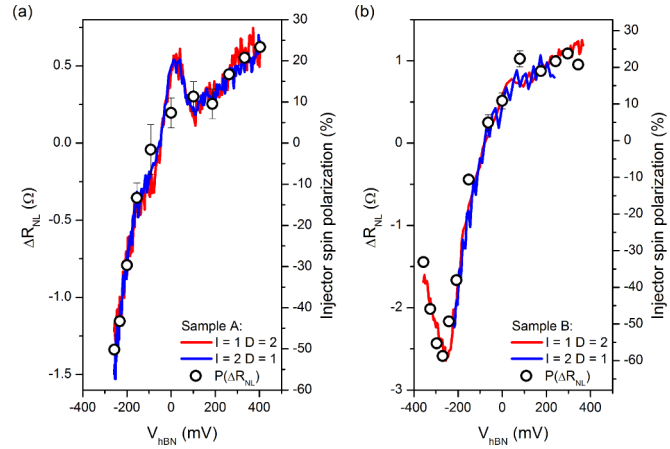

FIG. 3. Nonlocal spin transport in (a) sample A and (b) sample B for different dc bias voltages. For comparison, the dependence is shown as a function of the bias voltage applied across the hBN barrier. The blue and red curves correspond to the configuration where detector and biased injector contacts are swapped. The spin polarization on the right side of both panels is extracted from the independently measured ΔR_{NL}.

polarization via

$$P_{\mathrm{I}} P_{\mathrm{D}} = \frac{\Delta R_{\mathrm{NL}} w}{R_{\mathrm{sq}} \lambda} e^{-d/\lambda}, \tag{1}$$

where ΔR_{NL} is the spin signal, w is the width of the flake, R_{sq} is the square resistance, λ is the spin relaxation length, and d is the injector to detector distance measured from the centers. Under the assumption that $P_{\mathrm{I}} = P_{\mathrm{D}}$ we obtain an unbiased spin polarization of 14.65% for sample A and 10.86% for sample B. Because we apply the dc bias only to the injector contact, the spin polarization of the detector remains constant and can be used to extract the dependence of the differential spin injection polarization on the dc bias. We note that the feature of sample A around zero dc bias does not appear on all contacts on sample A (3 out of 5) and does not appear on sample B [30].

IV. BIAS-DEPENDENT SPIN PRECESSION MEASUREMENTS AND ESTIMATION OF THE PROXIMITY INDUCED EXCHANGE FIELD IN BL-HBN/GRAPHENE/YIG

To estimate the strength of the induced exchange field, we apply and rotate a small magnetic field ($B = 15$ mT) in the sample plane [Fig. 4(a)]. The low in-plane coercive field of the YIG films allows us to rotate the YIG magnetization and simultaneously the proximity induced exchange field while leaving the magnetization of the cobalt injector and detector unaffected. The resulting modulation of the nonlocal resistance is a direct consequence of $B + B_{\mathrm{exch}}$ and can be only explained by the presence of such [14,15].

The analysis of this effect gives us an estimate for the strength of the exchange field and allows us the fitting of the Hanle curves to extract further spin transport parameters. Note that we attribute the random oscillations that remain in the symmetrized data in Fig. 4(b) to either present temperature instabilities of the measurement setup or sample drift.

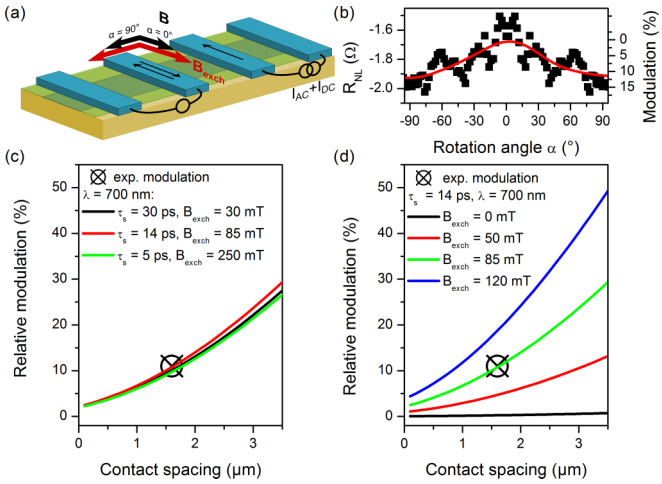

FIG. 4. Modulation of spin transport with the exchange field in sample A. (a) Schematics of the experiment. B is rotating the YIG magnetization and the exchange field B_{exch} in the sample plane while leaving the electrodes and injected spins unaffected. (b) The angle dependence of the nonlocal resistance $[\Delta R_{\mathrm{NL}} = R_{\mathrm{NL}}(\mathrm{P}) - R_{\mathrm{NL}}(\mathrm{AP})]$ is measured at $T = 10$ K and -20 μA dc bias in parallel and antiparallel alignment. The subtracted spin signal is symmetrized. As a guide to the eye the smoothed data is shown in red, from which we estimate a relative modulation of 11%. (c) Fitting of the experimental relative modulation of 11% with our model using τ_s and B_{exch} as fitting parameters. $\lambda = 700$ nm and $B = 15$ mT are fixed parameters. (d) Relative modulation of the spin signal calculated from the model using best fit parameters $\tau_s = 14$ ps and $\lambda = 700$ nm, obtained as shown in Fig. 5. B_{exch} is varied as indicated, and $B = 15$ mT.

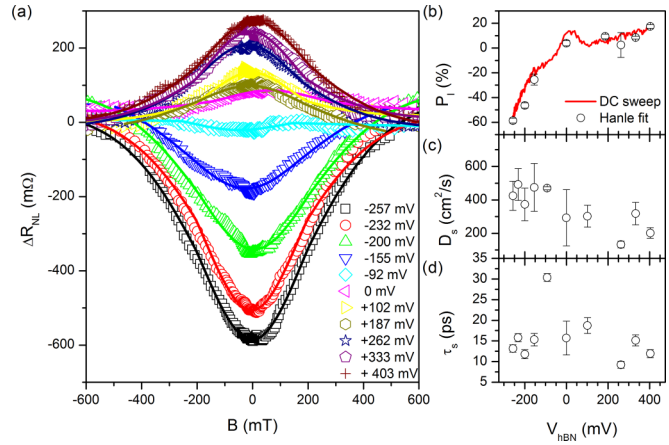

FIG. 5. Spin precession measurements in sample A: (a) The Hanle spin precession curves from sample A are fit using our exchange model with $B_{\mathrm{exch}} = 85$ mT (solid lines) for different dc bias currents. Contact 1 is used as an injector, contact 2 as a detector [Fig. 2(a)]. We extract (b) the calculated spin polarization the injector (P_{I}), (c) the spin diffusion coefficient D_s, and (d) the spin diffusion time τ_s. The dc bias dependence P_{I} shows a similar dependence as red line in (b), Fig. 3(d).

Therefore, we apply a smoothing on the data, the resulting curve is shown in red. We estimate the modulation to be (11 ± 5)% over $d = 1.6$ μm, which, given the uncertainty arising from the smoothing process, should be seen as a rather rough approximation. Despite the uncertainty of the exact value of the modulation, the angular dependence indicates the presence of an exchange field in the sample.

Using the model reported in Leutenantsmeyer *et al.* [14] we can simulate the modulation of a spin current by exchange field induced precession. To estimate the magnitude of the exchange field leading to 11% modulation, we use $\lambda = 700$ nm [Fig. 2(d)] and assume τ_s to be between 5 and 30 ps, a common range for our single layer graphene devices on YIG. To match the experimental modulation, an exchange field between 0 and 250 mT is required [Fig. 4(c)]. To determine the exact value of τ_s, we use the parameter pairs of τ_s and B_{exch} to fit, as discussed later, the spin precession measurements in Fig. 5(a). By comparing both, we find that both measurement sets can only be fit consistently with $\tau_s = 14$ ps and $B_{\mathrm{exch}} = 85$ mT.

Figure 4(d) contains the modulation caused by the combination of the applied magnetic field of 15 mT and different values for the exchange field. The expected relative modulation caused by an applied magnetic field of 15 mT with $\lambda = 700$ nm and $\tau_s = 14$ ps does not exceed 0.5%, whereas the observed modulation is clearly larger. To fit the experimentally found modulation of 11%, we have to assume $B_{\mathrm{exch}} = 85$ mT. This is a strong indication for the presence of an exchange field in this device. We can conclude that within the uncertainty range of the relative modulation of (11 ± 5)%, the exchange field in sample A is (85 ± 35) mT.

The Hanle measurements are carried out in parallel and antiparallel alignment of the injector (contact 1) and detector (contact 2), see Fig. 2(a) for the contact labeling. We extract the spin signal by calculating $[R_{\mathrm{NL}}(\mathrm{P}) - R_{\mathrm{NL}}(\mathrm{AP})]/2$, shown in Fig. 5(a). From the Hanle fit using an exchange field of 85 mT, we extract the polarization of the injector P_{I} [Fig. 5(b)], the spin diffusion coefficient D_s [Fig. 5(c)], and the spin diffusion time τ_s [Fig. 5(d)]. While $D_s = (350 \pm 65)$ cm^2/s and $\tau_s = (16 \pm 5)$ ps remain approximately constant over the applied dc bias range we find a dependence of the injector spin polarization that resembles the dc bias dependence of the injector [Fig. 3(a)], which implies a consistency in the analysis. Using the spin diffusion coefficient D_s and time τ_s extracted from the Hanle measurements, we can calculate the spin relaxation length $\lambda = \sqrt{D_s \tau_s} = (730 \pm 230)$ nm. When compared to the estimation from the distance-dependent spin valve measurements [Fig. 2(a)] both approaches yield similar values which indicates again the consistency of the analysis.

Note that the rather smooth Hanle curves shown in Fig. 5(a) could be also fit with a conventional spin precession model that does not include any exchange field. These fittings yield $\tau_s \sim 25$ ps, $D_s \sim 800$ cm^2/s, and $\lambda \sim 1.4$ μm. Apart from D_s being unrealistically large, the extracted λ is two times larger than the result from the independently measured distance-dependent spin valves [Fig. 2(d)] which suggests that the fit of our results with the conventional model is unreliable. Furthermore, if we want to fit the modulation in Fig. 4(b) with $\lambda = 1.4$ μm and $\tau_s = 25$ ps, an exchange field of $\sim$60 mT would be required to match the data, even though the Hanle fitting did not include any B_{exch}. In return, the parameter sets that match 11% modulation do not fit the spin precession measurements unless the values are close to $\lambda = 700$ nm,

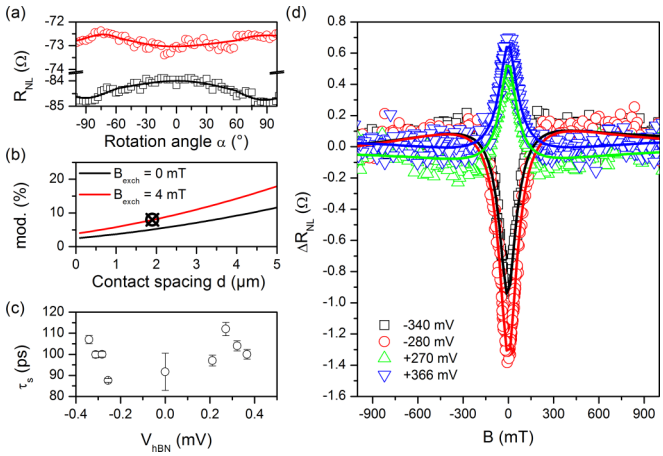

FIG. 6. (a) The nonlocal resistance can be modulated by 8% by rotating an in-plane magnetic field of 15 mT. The solid lines are smoothed and a guide to the eye. The red line is measured in parallel alignment, the black line in antiparallel configuration. (b) Modeling of the 8% modulation with the spin transport parameters of $\lambda = 2.3\ \mu$m and $\tau_s = 100$ ps. The black curve represents the modulation by the applied magnetic field of 15 mT in the absence of an exchange field, the red curve adds an exchange field of 4 mT. (c) The spin relaxation time τ_s extracted from the Hanle data in (d). (d) The Hanle spin precession curves of sample B with the fitting curves (lines) for different dc bias currents. The spin relaxation length of $\lambda = 2.3\ \mu$m is used as parameters for the fitting.

$\tau_s = 14$ ps, and $B_{\text{exch}} = 85$ mT. In conclusion, this analysis underlines the relevance to carry out both, angular modulation of R_{NL} and Hanle precession experiments, to characterize the exchange field strength.

V. BIAS-DEPENDENT SPIN PRECESSION MEASUREMENTS IN BL-HBN/BL-GRAPHENE/YIG

In comparison to sample A, sample B is fabricated with a bilayer graphene flake. The extraction of the spin relaxation length via distance-dependent spin valve measurements is done in a similar way as for sample A and is shown in the Supplemental Material [30]. We extract $\lambda = (2.3 \pm 1)\ \mu$m. The modulation of the nonlocal resistance by rotating the exchange field in the sample plane is shown in Fig. 6(a). The parallel (red) and antiparallel (black) data is measured at 10 K and -366 mV dc bias. The solid line is the smoothed data and used to estimate the relative modulation of the spin signal after subtraction of the parallel and antiparallel data which results in a modulation of 8%.

To estimate the exchange field causing this precession, we use $\lambda = 2.3\ \mu$m extracted for sample B from the distance-dependent measurements and assume $\tau_s = 100$ ps, which is later confirmed by the Hanle spin precession measurements. In this particular case, the modulation of the applied magnetic field of 15 mT [black line, Fig. 6(d)] already induces a modulation close to the experimentally found one. To match the data, a very small exchange field of only 4 mT would be required, leading us to the conclusion that in this device most likely no exchange interaction is present.

Using the Hanle spin precession data, we also extract $\lambda = 2.3\ \mu$m with a negligible exchange field. We find consistently over all biases a spin diffusion time of (100 ± 8) ps and a spin diffusion coefficient of $D_s = \lambda^2/\tau_s = (530 \pm 40)$ cm^2/s, which resembles the values used for the modulation fit and indicates consistency throughout our analysis of the spin transport. The possible absence of the exchange field in sample B stresses the importance of the graphene/YIG interface of these devices. This observation could be also explained with a different proximity effect on each of the two bilayer graphene layers. Nevertheless, sample B shows a similar dependence on the applied dc bias as sample A and shows that the tunable spin injection is also present in the bl-hBN/bl-graphene/YIG system.

VI. CONCLUSION

We have studied the spin injection through bl-hBN tunnel barriers into single and bilayer graphene on YIG, showing a more reliable and efficient spin injection compared to TiO_2 tunnel barriers. The bl-hBN tunnel barriers yield a resistance-area product between 5 and 30 k$\Omega\ \mu$m^2 and the spin injection polarization is found to be tunable through a dc bias current applied to the injector. We observe a sign inversion at approximately -80 mV dc bias applied across the bl-hBN flake. We estimate the proximity induced exchange field through in-plane and out-of-plane spin precession measurements to be around 85 mT in sample A and likely to be absent in sample B. The low magnitude of the exchange field compared to theoretical predictions emphasizes the importance of the graphene/YIG interface on the proximity induced exchange field and confirms our previously reported low exchange strength for graphene/YIG devices. Nevertheless, our results confirm the unique properties of bl-hBN for the reliable spin injection into single and bilayer graphene on YIG and stress the importance of this type of tunnel barrier for future application in graphene spintronics.

ACKNOWLEDGMENTS

We acknowledge the fruitful discussions with J. Ingla-Aynés, and funding from the European Unions Horizon 2020 research and innovation program under Grants No. 696656 and No. 785219 (Graphene Flagship core 1 and 2), the Marie Curie initial training network Spinograph (Grant No. 607904), and the Spinoza Prize awarded to B. J. van Wees by the Netherlands Organization for Scientific Research (NWO).

[1] A. K. Geim and I. V. Grigorieva, Nature (London) **499**, 419 (2013).

[2] W. Han, R. K. Kawakami, M. Gmitra, and J. Fabian, Nat. Nanotechnol. **9**, 794 (2014).

[3] S. Roche, J. Åkerman, B. Beschoten, J.-C. Charlier, M. Chshiev, S. Prasad Dash, B. Dlubak, J. Fabian, A. Fert, M. Guimarães, F. Guinea, I. Grigorieva, C. Schönenberger, P. Seneor, C. Stampfer, S. O. Valenzuela, X. Waintal, and B. J. van Wees, 2D Mater. **2**, 030202 (2015).
[4] J. H. Garcia, M. Vila, A. W. Cummings, and S. Roche, Chem. Soc. Rev. **47**, 3359 (2018).
[5] M. Gurram, S. Omar, and B. van Wees, 2D Mater. **5**, 032004 (2018).
[6] M. Drögeler, C. Franzen, F. Volmer, T. Pohlmann, L. Banszerus, M. Wolter, K. Watanabe, T. Taniguchi, C. Stampfer, and B. Beschoten, Nano Lett. **16**, 3533 (2016).
[7] T. Yamaguchi, R. Moriya, Y. Oki, S. Yamada, S. Masubuchi, K. Hamada, and T. Machida, Appl. Phys. Express **9**, 063006 (2016).
[8] M. Gurram, S. Omar, S. Zihlmann, P. Makk, C. Schönenberger, and B. J. van Wees, Phys. Rev. B **93**, 115441 (2016).
[9] W. Fu, P. Makk, R. Maurand, M. Bräuninger, and C. Schönenberger, J. Appl. Phys. **116**, 074306 (2014).
[10] M. V. Kamalakar, A. Dankert, J. Bergsten, T. Ive, and S. P. Dash, Sci. Rep. **4**, 6146 (2015).
[11] M. V. Kamalakar, A. Dankert, P. J. Kelly, and S. P. Dash, Sci. Rep. **6**, 21168 (2016).
[12] M. Gurram, S. Omar, S. Zihlmann, P. Makk, Q. C. Li, Y. F. Zhang, C. Schönenberger, and B. J. van Wees, Phys. Rev. B **97**, 045411 (2018).
[13] D. Huertas-Hernando, F. Guinea, and A. Brataas, Phys. Rev. B **74**, 155426 (2006).
[14] J. C. Leutenantsmeyer, A. A. Kaverzin, M. Wojtaszek, and B. J. van Wees, 2D Mater. **4**, 014001 (2017).
[15] S. Singh, J. Katoch, T. Zhu, K.-Y. Meng, T. Liu, J. T. Brangham, F. Yang, M. E. Flatté, and R. K. Kawakami, Phys. Rev. Lett. **118**, 187201 (2017).
[16] P. Wei, S. Lee, F. Lemaitre, L. Pinel, D. Cutaia, W. Cha, F. Katmis, Y. Zhu, D. Heiman, J. Hone, J. S. Moodera, and C.-T. Chen, Nat. Mater. **15**, 711 (2016).
[17] Z. Wang, C. Tang, R. Sachs, Y. Barlas, and J. Shi, Phys. Rev. Lett. **114**, 016603 (2015).
[18] P. Asshoff, J. Sambricio, A. Rooney, S. Slizovskiy, A. Mishchenko, A. Rakowski, E. Hill, A. Geim, S. Haigh, V. Fal'Ko, I. Vera-Marun, and I. Grigorieva, 2D Mater. **4**, 031004 (2017).
[19] Y. Song, J. Phys. D **51**, 025002 (2018).
[20] H. X. Yang, A. Hallal, D. Terrade, X. Waintal, S. Roche, and M. Chshiev, Phys. Rev. Lett. **110**, 046603 (2013).
[21] A. Hallal, F. Ibrahim, H. X. Yang, S. Roche, and M. Chshiev, 2D Mater. **4**, 025074 (2017).
[22] M. Evelt, H. Ochoa, O. Dzyapko, V. E. Demidov, A. Yurgens, J. Sun, Y. Tserkovnyak, V. Bessonov, A. B. Rinkevich, and S. O. Demokritov, Phys. Rev. B **95**, 024408 (2017).
[23] S. Pütter, S. Geprägs, R. Schlitz, M. Althammer, A. Erb, R. Gross, and S. T. B. Goennenwein, Appl. Phys. Lett. **110**, 012403 (2017).
[24] G. Schmidt, D. Ferrand, L. W. Molenkamp, A. T. Filip, and B. J. van Wees, Phys. Rev. B **62**, R4790 (2000).
[25] E. I. Rashba, Phys. Rev. B **62**, R16267(R) (2000).
[26] M. Gurram, S. Omar, and B. J. van Wees, Nat. Commun. **8**, 248 (2017).
[27] J. C. Leutenantsmeyer, J. Ingla-Aynés, M. Gurram, and B. J. van Wees, arXiv:1808.00904.
[28] T. Zhu, S. Singh, J. Katoch, H. Wen, K. Belashchenko, I. Žutic, and R. K. Kawakami, Phys. Rev. B **98**, 054412 (2018).
[29] P. J. Zomer, M. H. D. Guimarães, J. C. Brant, N. Tombros, and B. J. van Wees, Appl. Phys. Lett. **105**, 013101 (2014).
[30] See Supplemental Material at http://link.aps.org/supplemental/10.1103/PhysRevB.98.125422 for additional details on the sample characterization.
[31] Y. Hattori, T. Taniguchi, K. Watanabe, and K. Nagashio, ACS Nano **9**, 916 (2015).